

# Standard Penetration Testing in a virtual calibration chamber

Ningning Zhang<sup>a,\*</sup>; Marcos Arroyo<sup>a</sup>; Matteo Oryem Ciantia<sup>b</sup>; Antonio Gens<sup>a</sup>; Joanna Butlanska<sup>a</sup>

<sup>a</sup> *Department of Geotechnical Engineering and Geosciences, Technical University of Catalonia (UPC), SPAIN*

<sup>b</sup> *School of Science and Engineering, University of Dundee, UK*

\*Corresponding author at: Department of Geotechnical Engineering and Geosciences, Technical University of Catalonia (UPC), SPAIN. E-mail address: [ningning.zhang@upc.edu](mailto:ningning.zhang@upc.edu) (N. Zhang)

## ABSTRACT

The virtual calibration chamber technique, based on the discrete element method, is here applied to study the standard penetration test (SPT). A macro-element approach is used to represent a rod driven with an impact like those applied to perform SPT. The rod is driven into a chamber filled with a scaled discrete analogue of a quartz sand. The contact properties of the discrete analogue are calibrated simulating two low-pressure triaxial tests. The rod is driven changing input energy and controlling initial density and confinement stress. Energy-based blowcount normalization is shown to be effective. Results obtained are in good quantitative agreement with well-accepted experimentally-based relations between blowcount, density and overburden. It is also shown that the tip resistance measured under impact dynamic penetration conditions is close to that under constant velocity conditions, hence supporting recent proposals to relate CPT and SPT results.

**KEYWORDS:** Discrete element method; Standard penetration test; Blowcount; Energy; Fontainebleau sand

21 **List of notations**

- 22  $\sigma_{max}$  peak compressive stress in impact waves
- 23  $\mu$  friction coefficient
- 24  $\Delta\rho$  penetration depth per blow
- 25  $\rho_r$  mass density of rod material
- 26  $\nu$  Poisson's ratio
- 27  $\eta_d$  impact or dynamic efficiency ratio
- 28 I, II, III, IV and V phases in dynamic process
- 29  $a$  cross-sectional area of rod
- 30  $A_h$  cross-sectional area of hammer
- 31  $B$  and  $C$  material dependent parameters
- 32  $c$  wave propagation velocity in rod
- 33  $d_1$  and  $d_2$  diameters of the two spheres in contact
- 34  $d_c$  rod outside diameter
- 35  $D$  coefficient
- 36  $D_c$  chamber diameter
- 37  $D_r$  relative density
- 38  $D_{50}$  mean grain size
- 39  $e_{max}$  maximum void ratio
- 40  $e_{min}$  minimum void ratio
- 41  $E$  elastic modulus of rod material
- 42  $E_{blow}$  energy delivered by hammer to driven rod
- 43  $ER$  ratio of energy delivered by hammer to theoretical driving energy
- 44  $F_{max}$  maximum impact force
- 45  $F_n$  impact force for  $n$ th ( $n > 1$ ) compression pulse
- 46  $|F_n|$  magnitude of normal contact force
- 47  $F_{p-j}^t$  vertical reaction from particle  $j$  at rod tip at time  $t$
- 48  $F_{s-i}^t$  vertical reaction force from particle  $i$  along shaft at time  $t$
- 49  $F_{tot}^t$  total force acting on rod at time  $t$
- 50  $F_{drv}^t$  imposed driving force at time  $t$

51	$g$	gravitational acceleration
52	$G$	shear modulus
53	$G_r$	gravitational force of rod
54	$h$	falling height of hammer
55	$H$	chamber height
56	$k_n$	normal contact stiffness
57	$k_s$	shear contact stiffness
58	$l$	length of rod
59	$L$	length of hammer
60	$m_h$	hammer mass
61	$m_r$	rod mass
62	$n_p$	rod/particle ratio
63	$N$	SPT blow counts
64	$N_{60}$	dynamic resistance normalized by 60% energy efficiency
65	$P_0$	confining pressure
66	$q_d$	dynamic tip resistance
67	$q_e$	static tip resistance
68	$r$	hammer-rod impedance ratio
69	$R_d$	chamber/rod ratio
70	$\Delta t$	timestep
71	$t$	time duration of each compression wave
72	$t_{max}$	maximum impact time
73	$t_{eq}$	equilibration time
74	$t_1, t_2, t_3$ and $t_4$	characteristic time points identified in penetration curve
75	$U$	sphere overlap
76	$U_R$	rod potential work
77	$v_{peak}$	rod peak velocity
78	$v_r(t)$	driven rod velocity history
79	$V_h$	velocity of hammer at impact
80	$W_H$	hammer input work
81	$\dot{x}^{i+\Delta t}$	velocity component of rod

- 82  $\dot{z}^t$  vertical velocity of rod at time  $t$
- 83  $\dot{z}^{t+\Delta t}$  vertical velocity of rod at time  $(t+\Delta t)$

## 84 1. INTRODUCTION

85 Dynamic probing involves driving a device into the soil by striking it with a hammer. This technique is  
86 employed in several site investigation tests such as the Standard Penetration Test (SPT), Becker Penetration  
87 Test (BPT), Dynamic Cone Penetration Test (DCPT) or light dynamic penetrometers (e.g. Panda; [1]). Of  
88 these, the Standard Penetration Test (SPT) remains as one of the most popular in-situ testing procedures  
89 [2], frequently used to estimate soil properties [62, 18], foundation design parameters and evaluate  
90 liquefaction potential [49].

91 Tests based on dynamic probing have several advantages: they are widely available, economical and robust.  
92 They can be used in any ground condition, particularly on coarse materials such as gravels, ballast or  
93 weathered rock, where most alternatives fail. Dynamic probing tests also have important limitations. First:  
94 they are difficult to control precisely, which is detrimental for test repeatability. Second: they usually  
95 produce a single measurement per test (for instance  $N$ , number of blows to drive a sampler 300 mm in the  
96 ground) and such a restricted output inherently limits interpretation. Third: the mechanics of their  
97 interaction with the ground are poorly understood, which forces interpretation by strictly empirical  
98 approaches. All these shortcomings have been addressed in previous research, but to a different extent.

99 Many efforts have concentrated in improving test control and repeatability. A major step in this direction  
100 was made when energy input measurements were developed for the SPT [3, 4]. Recording the energy input  
101 from hammer blows on the rod-sampler system allowed to introduce an energy normalized blow number,  
102  $N_{60}$ , which was shown to improve significantly test output repeatability [5, 6]. The energy-normalized value  
103  $N_{60}$  is now a required basis for quantitative SPT interpretation [7, 8]. Further research [9, 10, 11] has  
104 progressively refined the methodology applied to measure and extract the amount of energy actually  
105 delivered to the driven sampler. Energy input measurement techniques have been also developed for other  
106 dynamic probes, like the Panda or the BPT [12].

107 Several proposals are also available to increase the number of results obtained from each test. Some, like  
108 the torsional SPT or SPT-T [13], require extra specific procedural steps. Perhaps more interesting are those  
109 that obtain extra results from the same procedure, for instance through interpretations of SPT based on  
110 penetration per blow,  $\Delta\rho$ , [2] or enhanced dynamic data acquisition for light dynamic penetrometers [14].

111 Testing under well controlled conditions is essential to understand the factors underlying the dynamic  
112 interaction between probes and soils. In the laboratory in situ tests are typically studied using calibration  
113 chambers. Because of the complexities involved, comparatively little calibration chamber work on dynamic  
114 driven probes has been reported [15, 16, 17]. Experimental data supporting dynamic test interpretation is  
115 then mostly gathered from field studies, [6, 18]. Unfortunately, field studies are costly, slow and subject to  
116 numerous uncertainties.

117 In principle, numerical simulation may be also used to perform controlled dynamic probing experiments.  
118 This, however, is difficult to put into practice, since dynamic probing involves large displacements, large  
119 strains, moving boundaries and high loading frequencies. It is not clear which numerical technology will  
120 be more appropriate for this kind of study. For granular soils, models based on the Discrete Element Method  
121 (DEM) [19] appear attractive because 1) they are able to deal with large displacement contact problems in  
122 a dynamic setting, 2) they have relatively few free material parameters to calibrate, and 3) they can easily  
123 incorporate grain scale properties such as crushability, which are known to strongly affect the results of  
124 dynamic probing tests [20].

125 The use of 3D DEM models to create virtual calibration chambers (VCC) is well established for quasi-static  
126 tests like the cone penetration test (CPT) [21, 22, 23, 24] or the Marchetti dilatometer [25]. VCC for light

127 dynamic penetrometers have been used by Breul and co-workers, mostly using 2D models [26, 27] but  
128 sometimes also in 3D [28]. A similar approach has been also recently used to study the impact of torpedo  
129 anchors [29].

130 The objective of this work is to demonstrate the potential of the DEM virtual calibration chamber technique  
131 to study standard penetration testing in granular soils. In previous VCC studies [21, 23, 25] a specific  
132 physical test series has been selected for comparison. For the case of SPT such approach was not possible  
133 because the old key studies [15, 16] lacked energy measurements while more contemporary research [17]  
134 was too succinctly described. Furthermore, directly mimicking these studies would have required  
135 simulation of a borehole excavation phase, which introduces distracting complications. It was then decided  
136 to validate the VCC method in this case by examining if the results obtained for a more generic case would  
137 fit into well-established general empirical trends.

138 **In the following sections we describe how a 3D VCC model was built, filled with a calibrated discrete**  
139 **analogue of a representative quartz sand and then subject to a series of dynamic probes at varying**  
140 **confinement and density. The results obtained are then quantitatively compared with the existing physical**  
141 **database. The methodology employed to build the model is described in detail, paying particular attention**  
142 **to those aspects involved in the specification of the dynamic driving force. For reasons of space, the work**  
143 **presented here will focus on macro-scale results, leaving aside for the moment the possibilities of DEM**  
144 **models to explore the microscale [30].**

145

## 146 2. MODEL DESCRIPTION

### 147 2.1 A DISCRETE ANALOGUE OF FONTAINEBLEAU SAND

148

149 Fontainebleau sand is a standard test silica sand that has been extensively used in geotechnical research [31,  
150 32, 33]. Some of its physical properties are presented in Table 1.

151 **A discrete analogue of Fontainebleau sand is obtained using the DEM code PFC3D [34], which is employed**  
152 **in all the simulations described in this work. Particle crushing effects (e.g. [40]) are not included here, and**  
153 **the discrete elements employed are always unbreakable spheres. To roughly mimic the effect of non-**  
154 **spherical particle shapes, particle rotation was inhibited, directly fixing the rotational degrees of freedom**  
155 **of the particles. This simplified approach, can be traced back to Ting et al. [35] and was successfully applied**  
156 **in previous work with granular materials [21, 36, 37, 38, 39]. More refined consideration of particle shape**  
157 **effects may be obtained using rolling-resistance contact models (e.g. [41, 61]). However, such refinements**  
158 **complicate calibration and were thus left aside in this first exploratory study.**

159 The constitutive contact law describing force-displacement interaction between particles is elasto-plastic.  
160 A friction coefficient  $\mu$  defines the slip behavior at contacts. Contact rigidity is given by the ratio of contact  
161 forces and incremental displacements in the normal and tangential directions. In this study, the simplified  
162 Hertz-Mindlin theory is used to define the normal and tangential rigidity at each contact:

$$163 \quad k_n = \left( \frac{2\langle G \rangle \sqrt{2 \frac{d_1 d_2}{d_1 + d_2}}}{3(1-\langle \nu \rangle)} \right) \sqrt{U} \quad (1)$$

164

$$k_s = \left( \frac{2 \left( \langle G \rangle^2 3(1-\langle \nu \rangle) \frac{d_1 d_2}{d_1 + d_2} \right)^{1/3}}{2-\langle \nu \rangle} \right) |F_n|^{1/3} \quad (2)$$

165 Where,  $U$  is the sphere overlap,  $|F_n|$  is the magnitude of the normal contact force and the  $\langle \rangle$  brackets  
 166 indicate the mean value of the quantity considered of the contacting elements;  $G$  is the shear modulus,  $\nu$  is  
 167 the Poisson's ratio and  $d_1, d_2$  are the diameters of the contacting elements.

168 The contact model properties ( $G, \mu, \nu$ ) (Table 2) were taken from a previous calibration made by Ciantia et  
 169 al. [42]. Since a new version of the PFC software was employed here, the calibration set of triaxial  
 170 compression tests was simulated again. The numerical model response was thus compared anew with the  
 171 macroscopic responses of Fontainebleau sand in two low-pressure (100 kPa) triaxial compression tests  
 172 reported by Seif El Dine et al. [32]. The numerical tests were performed using a cubical cell of 4 mm in  
 173 size containing 11,000 elements. Element sizes for this cubical cell were selected to closely match the PSD  
 174 of Fontainebleau NE34 sand (Figure 1). The matching obtained (Figure 2) is considered adequate, given  
 175 the simplicity of the model.

176

## 177 2.2 CHAMBER CONSTRUCTION

178

179 The construction of 3-dimensional VCC models followed a procedure described previously [21, 23]. A  
 180 calibration chamber with 0.5 m height and 0.76 m diameter was built using wall elements. Discrete elements  
 181 filling up the chamber have the same contact properties and shape as those used for calibration. However,  
 182 to obtain a model with a manageable number of particles, their size was uniformly upscaled applying a  
 183 uniform scaling factor of 79, leading to a rod/particle ratio,  $n_p = 3.06$ , similar to that employed in previous  
 184 studies [21, 23]. The resulting size distribution is a shifted version of that **from the original sand** (Figure 1).  
 185 All the chamber boundaries were set to be frictionless.

186 Geometrical model details can be seen in Figure 3 and Table 3. The choice of chamber dimensions was  
 187 inspired by previous experimental work on the topic (see Table 4). In most of those studies, SPT was  
 188 performed at various locations within the chamber plan, apparently without major impact on the test results.  
 189 Here only testing at the axis of the chamber has been attempted. The resulting chamber/rod diameter ratio  
 190 is 15, a ratio that results in some chamber size effects for fully penetrating CPT (e.g. [30]). It is not clear  
 191 that such effects are equally relevant for the short dynamic probes performed here.

192 Tests were performed with the material in the chamber at pre-established values of density and isotropic  
 193 confinement. The radius expansion method (REM) was used to fill the chamber. To attain the target porosity,  
 194 inter-particle friction was reduced while all chamber walls were servo controlled to maintain an isotropic  
 195 compression of 5 kPa. After equilibration, inter-particle friction was reset to the calibrated value and  
 196 isotropic stress was ramped up to the target level. **In all simulations a local damping of 0.05 [43] was**  
 197 **employed and no viscous damping was considered.** Detailed energy balances of the VCC during driving  
 198 [44] show that such a small amount of damping results in negligible dissipation compared with that due to  
 199 contact friction.

200 A flat-ended rod of outside diameter 50.8 mm was created by using frictional rigid walls. Rod diameter has  
 201 been selected to coincide with the normalized dimension of the SPT sampling tube. A closed ended rod is  
 202 a feature of some dynamic probing tests, like the BPT, and may be also interpreted as representing a plugged

203 SPT sampler. Sampler plugging in sand has been assumed in previous SPT interpretation methods [2].  
 204 Realistic modelling of the plugging phenomenon is beyond the scope of this work as would likely require  
 205 applying a significantly smaller particle scaling factors. The contact model between rod and particles is also  
 206 a simplified Hertz-Mindlin with limiting friction. The parameters for the rod are given in Table 2. The entire  
 207 rod surface is assumed frictional.

208 During rod penetration, the VCC radial boundary was maintained at constant radial stress using a servo-  
 209 mechanism. The same stress level was also maintained at the top horizontal boundary. On the other hand,  
 210 the bottom horizontal boundary was fixed and no displacement was allowed.

211 When performing a SPT the first 15 cm of penetration are described as a seating drive, and not considered  
 212 when evaluating the test result. A similar procedure was employed here and the rod was firstly pushed into  
 213 the sample at a constant rate of 40 cm/s until the tip reached a depth of 15 cm. This also had the advantage  
 214 of minimizing any major influence of the top boundary during driving [30]. On the other hand, simply  
 215 stopping static penetration will result in locked-in residual forces against the rod. Therefore, after the 15  
 216 cm static penetration phase, a servo control was applied to slightly pull back the rod from the sample,  
 217 restoring the vertical total force on the rod to zero (see example in Figure 4). At this point, the model was  
 218 deemed to be in an appropriate state for launching dynamic penetration.  
 219

## 220 2.3 DYNAMIC DRIVING

### 221 2.3.1 REPRESENTATION OF DRIVEN RODS

222

223 Different approaches have been used to mimic driven rods in DEM simulations. Escobar et al. [26], using  
 224 2D DEM, represented a solid steel rod using bonded particles. This allows to model elastic wave  
 225 propagation through the rod. On the other hand, and because of the large contact rigidity necessary to model  
 226 steel, the time step required by the explicit time integration method becomes very small, and large  
 227 computational costs are incurred.

228 A computationally less costly alternative [28] is to represent the rod using a macro-element. This was done  
 229 here by bundling walls together and imposing on them a uniform rigid-body motion that approximates that  
 230 of the rod. The wall-bundle is forced to move vertically and, to ensure a dynamically correct motion, the  
 231 following equation is used:

$$232 \quad \dot{z}^{t+\Delta t} = \dot{z}^t + \frac{F_{tot}^t}{m_r} \Delta t \quad (3)$$

233 Where,  $\dot{z}^{t+\Delta t}$  and  $\dot{z}^t$  are the vertical velocities of rod at time  $(t+\Delta t)$  and  $t$ , respectively,  $\Delta t$  is the time step  
 234 and  $m_r$  is an assigned rod mass (see below).  $F_{tot}^t$  is the total force acting on the rod, i.e.

$$235 \quad F_{tot}^t = \sum_i F_{s\_i}^t + \sum_j F_{p\_j}^t + F_{drv}^t + m_r g \quad (4)$$

236 Where,  $F_{s\_i}^t$  is the vertical reaction force from particle  $i$  along the shaft,  $F_{p\_j}^t$  is the vertical reaction from  
 237 particle  $j$  at the rod tip,  $F_{drv}^t$  is an imposed driving force and  $g$  is the gravitational acceleration.

238 The virtual rod mass,  $m_r$  is determined from values of rod length  $l$  and rod material density  $\rho_r$  that are  
 239 assigned in the specification of the imposed driving force.

240

### 241 2.3.2 SPECIFICATION OF DRIVING FORCE

242

243 In Eq (4), a time-dependent force input is specified to represent the driving force. The force input employed  
244 in this work was intended to approximate the characteristics of an SPT blow.

245 Recent experimental work [45, 46] indicates that a single SPT blow may result in relatively complex time-  
246 force signals in the rod, with several impacts due to hammer rebound and/or hammer delay and subsequent  
247 catch-up. The characteristics of the input force are thus strongly dependent on the particularities of the  
248 driving mechanism and the soil nature. Structural dynamic 1D models may be used to predict input force  
249 characteristics for a particular configuration of the impact mechanism [3, 10]. Such approaches seemed  
250 unnecessarily complex for the exploratory work presented here. Instead, a relatively simple but realistic  
251 input force was derived from a simplified hammer-rod interaction analysis. Fairhurst [47] proposed an  
252 elastodynamic model to describe the time history of an ideal impact force between a hammer and a rod. It  
253 assumes cylindrical pieces, no separation between hammer and rod and takes into account the transmission,  
254 at the hammer/rod interface, of rebound waves from the upper hammer end as successive compression  
255 pulses of progressively reduced stress levels.

256 According to this model the peak compressive wave stress during the first impact,  $\sigma_{max}$ , is given by

$$257 \quad \sigma_{max} = \rho_r c \left( \frac{V_h}{1+r} \right) \quad (5)$$

258 Where,  $c$  is the wave propagation velocity in the rod,  $V_h$  is the hammer impact velocity, and  $r$  is the hammer-  
259 rod impedance ratio, equal to the ratio of cross-sectional area of the rod,  $a$ , to the area of the hammer  $A_h$ , if  
260 both are of the same material. The wave propagation velocity is calculated as

$$261 \quad c = \sqrt{E / \rho_r} \quad (6)$$

262 Where,  $E$  is the elastic modulus of the rod material. The hammer impact velocity is here calculated through

$$263 \quad V_h = \eta_d \sqrt{2gh} \quad (7)$$

264 Where,  $h$  is the falling height of hammer and  $\eta_d$  represents a dynamic efficiency ratio. Unless otherwise  
265 stated, in all the simulations below, the value of this parameter is always set as 1. From the relations above  
266 it follows that the maximum impact force can be expressed as

$$267 \quad F_{max} = \frac{\eta_d a \sqrt{2ghE\rho_r}}{1 + \left( \frac{a}{A_h} \right)} \quad (8)$$

268 The corresponding impact force  $F_n$  for the  $n$ th ( $n > 1$ ) compression pulse, is

$$269 \quad F_n = F_{max} \left( \frac{1-r}{1+r} \right)^{n-1} \quad \text{for} \quad \frac{2(n-1)L}{c} < t < \frac{2nL}{c} \quad (9)$$

270 Where,  $L$  is the hammer length and  $t$  defines the time duration of each compression wave.

271 The simulated impact is terminated at time  $t_{max} = 2l/c$  after the start of impact, where  $l$  is the length of rod.  
 272 This would be the time when an elastic wave reflected from the rod tip as a tension wave returns to the rod  
 273 head and pulls it away from the hammer. The maximum number of completed stress steps  $n$  before loss of  
 274 hammer contact is then given by the integer part of  $l/L$ . In experimental records of SPT blows, [3, 46], this  
 275 round-trip time  $t_{max}$  coincides, approximately, with the duration of the first hammer impact which is that  
 276 delivering the largest amount of energy to the sample.

277 The parameters describing the simulated driving system are collected in Table 5. The hammer and the rod  
 278 are assumed to be of the same steel material. The rod is assumed to be 10 m long. The hammer diameter is  
 279 assumed to be twice that of the rod and its length (approximately 1/10 of that if the rod) was computed from  
 280 its assumed mass and steel density. Using these inputs, a 63.5 kg hammer falling from a height of 0.76 m  
 281 will generate a 4 ms impact force with  $F_{max} = 251$  kN (Figure 5).

### 282 2.3.3 BLOWCOUNT, BLOW ENERGY AND ENERGY RATIO

283

284 The value of equivalent blow counts  $N$  is determined by the **ratio** of the reference 30 cm distance by the  
 285 penetration depth per blow  $\Delta\rho$ . Following a similar reasoning to that presented by Odebrecht et al. [11] the  
 286 energy delivered by the driven rod to the VCC in a given blow,  $E_{blow}$ , is computed as the sum of hammer  
 287 input work  $W_H$  and work done by the rod self-weight,  $U_R$ . These energy terms can be calculated by  
 288 integrating the work done by the impact force and gravitational forces on the driven rod,

$$289 \quad E_{blow} = W_H + U_R = \int_0^{t_{eq}} F_{drv}(t)v_r(t)dt + m_r g \int_0^{t_{eq}} v_r(t)dt \quad (10)$$

290 Where,  $v_r(t)$  represents the driven rod velocity history, which is an output of the test and the upper limit of  
 291 the integral,  $t_{eq}$  is the time for equilibration.

292 Following standard practice, an energy ratio is then computed normalizing the energy delivered by the  
 293 theoretical driving energy of an SPT (given by a hammer mass,  $m_h = 63.5$  kg; fall height  $h = 0.76$  m)

$$294 \quad ER = \frac{E_{blow}}{m_h gh} \quad (11)$$

295 Depending on various hammer types and testing details, the energy ratio in practical field testing can vary  
 296 in a wide range from 30% to 90% [5, 6, 11, 48]. It has become common practice to normalize the blow  
 297 count, taking into account the energy ratio delivered to obtain a standardized blow number  $N_{60}$   
 298 (corresponding to blows of 60% energy efficiency) as:

$$299 \quad N_{60} = \frac{ER}{60} N \quad (12)$$

300

## 301 2.4 SIMULATION PROGRAM

302

303 The main soil state variables affecting dynamic penetration results are density and stress level. These are  
 304 represented here by relative density  $D_r$  and mean confining pressure  $P_0$ . The specimens were generated by  
 305 combining four density levels, namely very dense ( $D_r=82\%$ ), dense ( $D_r=72\%$ ), medium ( $D_r=60.5\%$ ) and  
 306 loose ( $D_r=38.6\%$ ) and three confining stress levels ( $P_0=100$  kPa, 200 kPa and 400 kPa). A series of impact

307 tests were conducted in all the 12 specimens by prescribing the same force-time signal proposed previously.  
308 The main characteristics of these DEM-based tests are collected in Table 6.

309

### 310 3. RESULTS

311 Even restricting ourselves to the macroscopic level, a wealth of results are available, since tip resistance,  
312 hammer input energy, rod motion features are continuously tracked in time. Before examining the effects  
313 of the main controlling variables on test results it is interesting to consider in detail the dynamics of a single  
314 blow.

315

#### 316 3.1 IMPACT DYNAMICS

317

318 The evolution in time of rod velocity, rod acceleration, rod tip position (i.e. penetration depth) and tip  
319 resistance is illustrated in Figure 6 for a representative example (test Loose\_200 in Table 6). The record  
320 was interrupted after 0.15 s, as most variables had by then reached a stationary value.

321 A dynamic penetration curve (Figure 7) can be deduced from the previous results by representing tip  
322 resistance vs dynamic penetration (i.e. rod penetration minus the 0.15 m achieved statically). The dynamic  
323 penetration curves obtained appear very similar to those registered using instrumented dynamic  
324 penetrometers [14, 26]. Several characteristic points are identified in the penetration curve, corresponding  
325 to times  $t_1$ ,  $t_2$ ,  $t_3$  and  $t_4$ . Using these characteristic times 5 phases (I, II, III, IV and V) are distinguished in  
326 the dynamic process (Figure 6).

327 The first phase (*I*; which might be called “*acceleration*”) corresponds to the period in which rod  
328 acceleration is negative (i.e. downwards), with  $t_1$  selected as the time in which acceleration first changes  
329 sign (Figure 6b). Until this moment the imposed driving force is overcoming the soil resistance acting on  
330 the rod. Rod velocity attains then its maximum at 1.4 m/s, a value close to the anvil velocities under SPT  
331 registered by Lee et al. [46]. Phase *I* is also characterized by a quasi-linear rise in tip resistance. Shortly  
332 after  $t_1$  the tip resistance begins to oscillate while penetration advances.

333 The second phase (*II*; “*deceleration*”) finishes when the velocity of the rod crosses zero at  $t_2$ . Of course, at  
334 this point penetration advance stops. In this phase soil resistance decelerates the rod with a relatively  
335 constant magnitude, hence reducing rod velocity at an almost constant rate. Penetration continues  
336 accompanied of large tip resistance oscillations -the largest of which is coincident with the only significant  
337 step in acceleration magnitude during this phase.

338 The third phase (*III*; “*unloading*”) corresponds to a period in which the rod rebounds and the tip is  
339 progressively unloaded until it becomes practically 0 at  $t_3$ . There is still some inertia in the system that is  
340 revealed in rod oscillations during phase *IV*, which lasts until the rod attains its final penetration depth at  $t_4$ .  
341 The rod was driven to a permanent penetration of 0.026 m, corresponding to a blow number  $N = 12$ . Beyond  
342 that time, in phase *V*, only small oscillations in the residual tip resistance are visible, perhaps best seen as  
343 an indication of a somewhat insufficiently damped system.

344

#### 345 3.2 PENETRATION AND DRIVING ENERGY

346

347 As recorded in Table 7 the energy ratios delivered to the chamber lie mostly within the 40% - 50% range.  
348 Those values are within the range of observed field energy ratios 30%-90% [49] although clustered towards  
349 the lower end. Note that, in the field, the energy delivered by a hammer blow frequently requires more time  
350 than the strict two-way rod wave trip time assumed here to establish  $t_{max}$ . Figure 8 plots the energy ratio  
351 levels and the penetration per blow observed for all the different tested conditions of density and confining  
352 stress. A proportionality between these two magnitudes is evident from the figure, **much like** that observed  
353 by Schnaid et al [50] in field testing.

354 The energy normalization of blowcount in equation (12) implies that the normalized value is independent  
355 of the driving system characteristics or, equivalently, that  $N_{60}$  is only affected by soil properties (parameters  
356 and state). As noted before that was verified empirically by field testing, driving SPT at the same site with  
357 different, independently measured, energies [3, 6]. It seemed reasonable to check if this energy  
358 normalization is also verified in the VCC. To this end, a separate series of simulations was run, modifying  
359 the driving force history by the simple expedient of using different values of the dynamic efficiency ratio,  
360  $\eta_d$  (0.7, 0.9, 1.0 and 1.2). All the other settings were maintained constant and therefore the driving time was  
361 kept constant at 4 ms. The different resulting force-time curves are illustrated in Figure 9.

362 The blows at different energy were simulated on specimen Dense\_100. The results are summarized in Table  
363 8 and both measured blowcounts,  $N$ , and normalized blowcounts  $N_{60}$  are presented in Figure 10. It is evident  
364 that the energy normalization **works well**, with all the normalized  $N_{60}$  values very close to one another.

365

### 366 3.3 INFLUENCE OF GROUND CONDITIONS ON PENETRATION RESISTANCE

367

368 There are a great number of soil-related factors known to influence the resistance to dynamic penetration,  
369 including void ratio, current stress levels, average particle size, coefficient of uniformity, particle angularity,  
370 cementation, aging, etc. For granular soils, however, a main focus has been always on establishing the  
371 relation between SPT blow count and relative density.

372 It was early noticed that, although the influence of relative density on SPT was very strong, it could not be  
373 considered separately from that of stress level. In a classical study, Gibbs and Holtz [15] used calibration  
374 chamber testing to explore the relation between  $N$ , relative density ( $D_r$ ) and overburden pressure ( $P_0$ ). Their  
375 results for dry sands were summarized by Meyerhof [51] in the following relation

$$376 \quad N = 1.7 \times \left( \frac{D_r}{100} \right)^2 (0.145P_0 + 10) \quad (13)$$

377 where the overburden pressure  $P_0$  is expressed in kPa.

378 Later calibration chamber studies (Table 4) of SPT in sands have proposed slightly different formulations,  
379 generally indicating a feebler effect of relative density than that observed by Gibbs and Holtz [15].  
380 Differences are attributed [16, 17] to the effects of saturation, to details of the dynamic testing procedure  
381 or to fabric effects derived from specimen formation procedures (e.g. dynamic compaction vs pluviation).  
382 It is also clear that creating homogeneous tank-sized specimens of sand is a very difficult task, as shown by  
383 the large variability in results reported by Marcuson and Bieganouski [16].

384 Figure 11 compares the prediction of the summary equations proposed by different authors with the results  
385 obtained from the DEM simulations for the case in which  $P_0$  equals 200 kPa. The DEM results appear to

386 match very well the Meyerhof [51] expression. A more complete comparison with this classical  
387 experimental result is presented in Figure 12. It appears that the comparison deteriorates as the blow number  
388 increases, with the DEM simulation resulting in smaller blow-counts than those predicted by Meyerhof  
389 [51]. Because the blow energy applied by Gibbs and Holtz [15] was not measured it is difficult to pin down  
390 possible causes for this discrepancy, although it is likely that the numerical experiments delivered too little  
391 energy for the stronger specimens.

392 To avoid this kind of difficulty, Skempton [6] made a systematic effort to compare field and laboratory  
393 tests using only normalized blowcount. He found that the shape of the Meyerhof [51] expression was also  
394 valid when the normalized blowcount was employed, thus giving

$$395 \quad \frac{N_{60}}{D_r^2} = B + C \frac{P_0}{100} \quad (14)$$

396 Where  $B$  and  $C$  are material dependent parameters. Skempton [6] presented results indicating that, for  
397 normally consolidated sands, parameter  $B$  ranged between 17 and 46 and parameter  $C$  between 17-28.

398 Figure 13 presents the influence of overburden and relative density on the  $N_{60}$  values obtained from the  
399 simulations. The lineal influence of overburden and the quadratic influence of relative density are apparent  
400 in these results. When all the data is summarized in a single regression (Figure 14) it is observed that while  
401 the slope ( $C \sim 27$ ) is very much in line with Skempton [6] values, the intercept value ( $B = 5$ ) appears  
402 comparatively small. It should be noticed, however, that the field values quoted by Skempton [6] did carry  
403 significant uncertainty, as they were frequently obtained using reasonable guesses about the intervening  
404 variables (energy applied, efficiency, relative density or stress level). Figure 14 also includes the results  
405 obtained using downhole frozen samples by Hatanaka and Uchida [52]. It is noticeable how these  
406 experimental results also cluster in the low intercept range.

407

#### 408 **4. DYNAMIC VS STATIC RESISTANCE**

409

410 It is interesting to compare the tip resistance obtained from the dynamic probes with the values that are  
411 obtained if the static penetration is continued to the same depths (Figure 15). Because of the large  
412 oscillations visible in the traces the comparison is best based on some representative statistics. The dynamic  
413 tip resistance  $q_d$  is thus obtained averaging the tip resistance measured during the “*deceleration*” phase  
414 (phase *II* in Figure 7). The reference static tip resistance  $q_e$  is obtained averaging the static tip resistance  
415 within the same depths. As illustrated in Figure 16a the mean values of dynamic and static tip resistances  
416 are very close to one another when they are below 10 MPa. Above this value the dynamic tip resistance is  
417 smaller than the static one. The 10 MPa limit also corresponds to a significant increase in the magnitude of  
418 dynamic oscillations of tip resistance, as indicated by the standard deviations plotted in Figure 16b.

419 When cone penetration is performed at constant velocity there is a marked increase in tip resistance when  
420 the push velocity increases above 1 m/s [27, 28]. This increase is due to inertial effects kicking in above  
421 that limit. The peak velocity in the dynamic probes performed here is always above that limit, but reduces  
422 as penetration resistance increases (Figure 17). Note also that the time fraction spent above this inertial  
423 velocity limit is relatively small, due to the fast deceleration occurring in phase II (Figure 6). It is therefore  
424 unclear how inertial effects, by themselves, may explain the observed discrepancy between static and  
425 dynamic penetration values.

426 Other factors that seem relevant for this issue are energy limits, blowrate and contact model effects. Figure  
427 18 illustrates the effect of density on the dynamic penetration curves at the highest confinement. It is evident  
428 that the plastic penetration at constant tip resistance that is characteristic of *phase II* is much reduced as  
429 density increases. It may be then inferred that in the denser more confined specimens the energy of the blow  
430 delivered was not enough to fully mobilized the available penetration resistance. Interestingly some of the  
431 tests in which the ratio  $q_d/q_e$  is smaller have blowcounts above or very close to the normalized limit for field  
432 test acceptance ( $N = 100$ ).

433 Blow-rate may be also involved. Schnaid et al [53] showed that, after properly accounting for the energy  
434 input in the dynamic test, the tip resistance in static and standard penetration tests had very similar values,  
435 a result independent of the resistance value. Schnaid et al [53] performed SPT according to the standard  
436 procedure, delivering blow after blow until 30 cm of penetration was achieved. On the other hand, the  
437 simulations presented here included a single blow. For fast blow-rates there may be an overlap in the  
438 mechanical effects of separate blows. Unfortunately blow-rate is neither prescribed in standard procedures  
439 nor typically recorded.

440 Finally, it should be noted that the contact model employed here has some limitations to represent load-  
441 unload cycles. A somewhat excessive elastic compliance is included to alleviate a simplified description of  
442 contact mechanics in which, for instance, roughness-induced effects [54] are not considered. The increased  
443 contact density of denser specimens would make this limitation more relevant, as can be seen in the  
444 continuation of rebound after unloading in the curves of Figure 18. Ongoing work is exploring how to  
445 alleviate this problem using more refined contact models, in which the effect of contact roughness is  
446 included [55].

447

## 448 5. CONCLUSIONS

449

450 This work set out to explore the capabilities of the DEM VCC approach to model SPT. In this respect, and  
451 despite the limitations noted for the higher density specimens, the main results obtained appear very positive.  
452 These are

- 453 • The macro-element approach may be applied to model a driving rod with a realistic driving force  
454 input.
- 455 • Input energy normalization has been shown to be as effective an approach as in field testing.
- 456 • The effects of density and overburden pressure are in good agreement with well-established  
457 empirically –based expressions.
- 458 • In blows that result on fully developed plastic penetration, a close correspondence between  
459 dynamic and static tip resistance is observed.

460 Even if continuum based simulation models are advancing fast [56, 57] it is our impression that DEM VCC  
461 models do offer some advantages for the case of dynamic probing. The macro-element approach allows for  
462 easy generalization to represent more realistic impact dynamics, for instance by coupling it with driving  
463 tool models such as those presented by Daniel and Howie [58]. Consideration of drainage effects is also  
464 possible with resource to complementary modelling techniques, (e.g. CFD-DEM coupling, [59, 60]). **But**  
465 **perhaps the most interesting applications will be those focusing on particle-scale influences on test result,**  
466 **such as grain crushing, gran size distribution effects or grain shape effects (either modelled directly or**

467 through a contact rolling resistance model). It is hoped that the work presented here will encourage those  
468 developments.

469

## 470 **6. ACKNOWLEDGEMENT**

471

472 The first author was supported by a CSC grant. This work was partly supported by the Ministry of Science  
473 and Innovation of Spain through the research grant BIA2017-84752-R and the EU H2020 RISE programme  
474 “Geo-ramp” (grant 645665).

475

476

477 **7. REFERENCES**

478

- 479 [1] Gourves, R., Barjot, R. (1995). "The Panda ultralight dynamic penetrometer". *Proceeding of*  
480 *ECSMFE*. Copenhagen, Denmark, 83-88.
- 481 [2] Schnaid, F., Odebrecht, E., Rocha, M. M., Bernardes, G. De P., (2009). "Prediction of Soil  
482 Properties from the Concepts of Energy Transfer in Dynamic Penetration Tests." *Journal of*  
483 *Geotechnical and Geoenvironmental Engineering* 135(May 2012): 1092–1100.
- 484 [3] Schmertmann, J. H., Palacios. A., (1979). "Energy Dynamics of SPT." *Journal of the Geotechnical*  
485 *Engineering Division* 105(GT8): 909–926.
- 486 [4] Kovacs, W. D., Salomone, L. A. (1982). "SPT hammer energy measurement". *Journal of*  
487 *Geotechnical and Geoenvironmental Engineering*, 108(GT4).
- 488 [5] Seed, H. Bolton, K. Tokimatsu, L. F. Harder, Riley M. Chung. (1985). "Influence of SPT  
489 Procedures in Soil Liquefaction Resistance Evaluations." *Journal of Geotechnical Engineering*  
490 111(12): 1425–1445.
- 491 [6] Skempton, A W. (1986). "Standard Penetration Test Procedures and the Effects in Sands of  
492 Overburden Pressure, Relative Density, Particle Size, Ageing and Overconsolidation."  
493 *Géotechnique*, 36(3), 425–47.
- 494 [7] CEN ISO 22476-3 (2005). "Geotechnical investigation and testing -- Field testing -- Part 3:  
495 standard penetration test"
- 496 [8] ASTM D1586 -11. (2011). "Standard Test Method for Standard Penetration Test (SPT) and Split-  
497 Barrel Sampling of Soils." In *Annual Book of ASTM Standards*, Philadelphia.  
498 papers2://publication/uuid/35B85424-852A-4B25-8883-63D2F4EF206B.
- 499 [9] Sy, A. Campanella, R. G., (1991) "An Alternative Method of Measuring SPT Energy".  
500 *International Conferences on Recent Advances in Geotechnical Earthquake Engineering and Soil*  
501 *Dynamics*. 2.
- 502 [10] Abou Matar, H., G. Goble. (1997). "SPT Dynamics Analysis and Measurements." *Geotechnical*  
503 *and geoenvironmental engineering*, 123(10), 921–928.
- 504 [11] Odebrecht, E., Schnaid, F., Rocha, M. M., de Paula Bernardes, G. (2005). "Energy Efficiency for  
505 Standard Penetration Tests". *Journal of Geotechnical and Geoenvironmental Engineering*, 131(10),  
506 1252–1263.
- 507 [12] DeJong, J. T., Ghafghazi, M., Sturm, A. P., Wilson, D. W., den Dulk, J., Armstrong, R. J., Davis,  
508 C. A. (2017). "Instrumented Becker Penetration Test. I: Equipment, Operation, and Performance".  
509 *Journal of Geotechnical and Geoenvironmental Engineering*, 143(9), 04017062.
- 510 [13] Décourt, L., Quaresma Filho, A. R. (1994). « Practical applications of the standard penetration test  
511 complemented by torque measurements, SPT-T: Present stage and future trends". In *Proceedings*  
512 *XIII ICSMFE*, New Delhi, Vol. 1, pp. 143-148. AA BALKEMA.
- 513 [14] Escobar, E. Benz, M. A., Gourvès, R., Breul, P. Chevalier, B. (2016) "In-situ determination of soil  
514 deformation modulus and the wave velocity parameters using the Panda 3®"; In *ISC5 Geotechnical*  
515 *and Geophysical Site Characterisation 5 –* Lehane, Acosta-Martínez and Kelly (Eds) 279-284
- 516 [15] Gibbs, H. J., Holtz, W. G. (1957). "Research on Determining the Density of Sands by Spoon  
517 Penetration Testing", *4th ICOSOMEF*, 1, 35-39

- 518 [16] Marcuson III, W. F., Bieganousky, W. A. (1977). "Laboratory standard penetration tests on fine  
519 sands". *Journal of Geotechnical Engineering Division*, 103(GT-6), 565–588
- 520 [17] Ishikawa, K, Atsushi I., Ogura, H. and Shimohira, Y. (2013). "Estimation of Sand N -Value Using  
521 Pressurized Sand Tank and Verification of Vertical Loading Test of Model Pile." *AIJ J. Technol.*  
522 *Des* 19(41): 107–112
- 523 [18] Hatanaka, M., and Feng, L. 2006. Estimating density of sandy soils. *Soils and Foundations J.* 46(3):  
524 299–314.
- 525 [19] Cundall, P A, and O. D. L. Strack. (1979). "A Discrete Numerical Model for Granular Assemblies."  
526 *Géotechnique* 29(1), 47–65
- 527 [20] Ahmed, S. M., Agaiby, S. W., and Abdel-Rahman, A. H. (2014). "A unified CPT–SPT correlation  
528 for non-crushable and crushable cohesionless soils". *Ain Shams Engineering Journal*, 5(1), 63-73
- 529 [21] Arroyo, M., Butlanska, J., Gens, A., Calvetti, F., Jamiolkowski, M. (2011). "Cone Penetration Tests  
530 in a Virtual Calibration Chamber." *Géotechnique*, 61(6): 525–531
- 531 [22] Zhang, Z., and Wang. Y., (2015). "Three-Dimensional DEM Simulations of Monotonic Jacking in  
532 Sand." *Granular Matter* 17(3), 359–376
- 533 [23] Ciantia, M. O., Arroyo, M., Butlanska, J., and Gens, A. (2016). "DEM modelling of cone  
534 penetration tests in a double-porosity crushable granular material". *Computers and Geotechnics*,  
535 73, 109-127
- 536 [24] Holmen, J. K., Olovsson, L., and Børvik, T. (2017). "Discrete modeling of low-velocity penetration  
537 in sand". *Computers and Geotechnics*, 86, 21-32
- 538 [25] Butlanska, J., Arroyo, M., Amoroso, S., and Gens, A. (2018). "Marchetti Flat Dilatometer Tests in  
539 a Virtual Calibration Chamber," *Geotechnical Testing Journal*, 41(5), 930-945
- 540 [26] Escobar, E., Benz, M., Gourvès, R., and Breul, P. (2013). "Dynamic cone penetration tests in  
541 granular media: Determination of the tip's dynamic load-penetration curve". In *AIP Conference*  
542 *Proceedings* (Vol. 1542, No. 1, pp. 389-392). AIP
- 543 [27] Tran, Quoc Anh, Bastien Chevalier, and Pierre Breul. (2016). "Discrete Modeling of Penetration  
544 Tests in Constant Velocity and Impact Conditions." *Computers and Geotechnics*, 71, 12–18.
- 545 [28] Quezada JC, Breul P, Saussine G, Radjai F. (2014) "Penetration test in coarse granular material  
546 using Contact Dynamics Method". *Comput Geotech*, 55, 248–253.
- 547 [29] Zhang, N., and Evans, T. M. (2019). "Discrete numerical simulations of torpedo anchor installation  
548 in granular soils". *Computers and Geotechnics*, 108, 40-52
- 549 [30] Butlanska, J., Arroyo, M., Gens, A., and O'Sullivan, C. (2014). "Multi-Scale Analysis of Cone  
550 Penetration Test ( CPT ) in a Virtual Calibration Chamber." *Canadian Geotechnical Journal* 51(1),  
551 51–66
- 552 [31] Plumelle, C., and Schlosser, F. (1991). "Three full-scale experiments of French project on soil  
553 nailing: CLOUTERRE". *Transp. Res. Rec*, (1330), 80-86
- 554 [32] Seif El Dine, B., Dupla, J. C., Frank, R., Canou, J., and Kazan, Y. (2010). "Mechanical  
555 characterization of matrix coarse-grained soils with a large-sized triaxial device". *Canadian*  
556 *Geotechnical Journal*, 47(4), 425-438
- 557 [33] Jardine, R J, Z X Yang, P Foray, and BT Zhu. (2013). "Interpretation of Stress Measurements Made

- 558 around Closed-Ended Displacement Piles in Sand.” *Géotechnique* 63(8): 613–627
- 559 [34] Itasca Consulting Group. (2016). PFC3D: Itasca Consulting Group, Inc. (2014) PFC — Particle  
560 Flow Code, Ver. 5.0 Minneapolis: Itasca Consulting Group.
- 561 [35] Ting, J. M., Corkum, B. T., Kauffman, C. R., and Greco, C. (1989). “Discrete numerical model for  
562 soil mechanics”. *Journal of Geotechnical Engineering*, 115(3), 379-398
- 563 [36] Calvetti, F., Di Prisco, C., and Nova, R. (2004). “Experimental and numerical analysis of soil–pipe  
564 interaction”. *Journal of geotechnical and geoenvironmental engineering*, 130(12), 1292-1299
- 565 [37] Ciantia M. O., Boschi K., Shire T., and Emam S. (2018) “Numerical techniques for fast generation  
566 of large discrete-element models”. Proceedings of the Institution of Civil Engineers - *Engineering  
567 and Computational Mechanics* 0 0:0, 1-15
- 568 [38] Zhang, N., Arroyo, M., Gens, A., and Ciantia, M. (2018a). DEM modelling of dynamic penetration  
569 in granular material. In *Numerical Methods in Geotechnical Engineering IX, Volume 1:  
570 Proceedings of the 9th European Conference on Numerical Methods in Geotechnical Engineering  
571 (NUMGE 2018)*, June 25-27, 2018, Porto, Portugal (p. 415). CRC Press.
- 572 [39] Zhang, N., Arroyo, M., Ciantia, M. and Gens. A., (2018b) DEM investigation of particle crushing  
573 effects on static and dynamic penetration tests. In *Proceedings of China-Europe Conference on  
574 Geotechnical Engineering (Wu W and Yu HS (eds))*. Springer, Cham, Switzerland, pp. 274–278
- 575 [40] Ciantia, M., Arroyo, M., Calvetti, F., and Gens, A. (2015). “An approach to enhance efficiency of  
576 DEM modelling of soils with crushable grains”. *Géotechnique*, 65(2), 91-110
- 577 [41] Rorato, R., Arroyo, M., Gens, A., Andò, E., Viggiani, G., 2018. “Particle shape distribution effects  
578 on the triaxial response of sands : a DEM study”, in: *Micro to MACRO Mathematical Modelling in  
579 Soil Mechanics*
- 580 [42] Ciantia, M. O., Arroyo, M., O'Sullivan, C., Gens, A., and Liu, T. (2018). “Grading evolution and  
581 critical state in a discrete numerical model of Fontainebleau sand”. *Géotechnique*, 1-15
- 582 [43] Cundall, P. A. (1987). “Distinct element models of rock and soil structure”. In *Analytical and  
583 computational methods in engineering rock mechanics* (ed. E. T. Brown), ch. 4, pp. 129–163.  
584 London, UK: Allen and Unwin
- 585 [44] Zhang, N (2019) Discrete element models of dynamic driving, PhD UPC (ongoing)
- 586 [45] Daniel, C. R., Howie, J. A., Jackson, R. S., and Walker, B. (2005). “Review of standard penetration  
587 test short rod corrections”. *Journal of geotechnical and geoenvironmental engineering*, 131(4),  
588 489-497
- 589 [46] Lee, C., Lee, J. S., An, S., and Lee, W. (2010). “Effect of secondary impacts on SPT rod energy  
590 and sampler penetration”. *Journal of geotechnical and geoenvironmental engineering*, 136(3), 522-  
591 526
- 592 [47] Fairhurst, C. (1961). “Wave Mechanics of Percussive Drilling.” *Mine and Quarry Engineering*  
593 27(4): 169–78
- 594 [48] Schmertmann, J. H. (1979). “Statics of SPT.” *Journal of the Geotechnical Engineering Division*  
595 105(5): 655–670
- 596 [49] Idriss, I. M., and R.W. Boulanger. (2008). “ Soil Liquefaction during Earthquakes”.
- 597 [50] Schnaid, F., Odebrecht, E., Lobo, B. O., and Rocha, M. M. (2009b). Discussion of “SPT Hammer

- 598 Energy Ratio versus Drop Height” by T. Leslie Youd, Hannah W. Bartholomew, and Jamison H.  
599 Steidl. *Journal of geotechnical and geoenvironmental engineering*, 135(11), 1777-1778
- 600 [51] Meyerhof, G. G. (1957). Discussion on Research on determining the density of sands by spoon  
601 penetratio testing. Proc. 4<sup>th</sup> Int. Conf. Soil Mech. Fdn Engng, London 3, 110.
- 602 [52] Hatanaka, M., & Uchida, A. (1996). Empirical Correlation between Penetration Resistance and  
603 Internal Friction Angle of Sandy Soils. *Soils and Foundations*, 36(4), 1–9.  
604 [https://doi.org/10.3208/sandf.36.4\\_1](https://doi.org/10.3208/sandf.36.4_1)
- 605 [53] Schnaid, F., Lourenço, D., and Odebrecht, E. (2017). “Interpretation of static and dynamic  
606 penetration tests in coarse-grained soils”. *Géotechnique Letters*, 7(2), 113-118
- 607 [54] Cavarretta, I., Coop, M., and O’Sullivan, C. (2010). “The influence of particle characteristics on  
608 the behaviour of coarse grained soils”. *Geotechnique*, 60(6), 413-423
- 609 [55] Otsubo, M., O’Sullivan, C., Hanley, K. J., and Sim. W. W., (2017), "The influence of particle  
610 surface roughness on elastic stiffness and dynamic response." *Geotechnique* 67(5), 452-459
- 611 [56] Monforte, L., Arroyo, M., Carbonell, J. M., and Gens, A. (2018). “Coupled effective stress analysis  
612 of insertion problems in geotechnics with the Particle Finite Element Method”. *Computers and  
613 Geotechnics*, 101, 114-129
- 614 [57] Moug, D.M., Boulanger, R.M., DeJong, J.T. and Jaeger, R.A. (2019), “Axisymmetric Simulations  
615 of Cone Penetration in Saturated Clay”, *Journal of Geotechnical and Geoenvironmental  
616 Engineering*, 145 (4)
- 617 [58] Daniel, C. R., and Howie, J. A. (2005). “Effect of hammer shape on energy transfer measurement  
618 in the Standard Penetration Test”. *Soils and Foundations*, 45(5), 121–126
- 619 [59] El Shamy, U., and Aydin, F. (2008). “Multiscale modeling of flood-induced piping in river levees”.  
620 *Journal of Geotechnical and Geoenvironmental Engineering*, 134(9), 1385-1398
- 621 [60] Climent, N., Arroyo, M., O’Sullivan, C., and Gens, A. (2014). “Sand production simulation  
622 coupling DEM with CFD”. *European Journal of Environmental and Civil Engineering*, 18(9), 983-  
623 1008. DOI: 10.1080/19648189.2014.920280
- 624 [61] Iwashita, K., & Oda, M. (1998). Rolling resistance at contacts in simulation of shear band  
625 development by DEM. *Journal of engineering mechanics*, 124(3), 285-292
- 626 [62] Hettiarachchi, H., & Brown, T. (2009). Use of SPT Blow Counts to Estimate Shear Strength  
627 Properties of Soils: Energy Balance Approach. *Journal of Geotechnical and Geoenvironmental  
628 Engineering*, 135(6), 830–834. [https://doi.org/10.1061/\(ASCE\)GT.1943-5606.0000016](https://doi.org/10.1061/(ASCE)GT.1943-5606.0000016)
- 629

630 **8. Tables**

631

632 Table 1 Physical properties of Fontainebleau sand

Database	$D_{50}$ : mm	$e_{min}$	$e_{max}$	$\rho_s$	$\rho_{d,min}$ : kN/m <sup>3</sup>	$\rho_{d,max}$ : kN/m <sup>3</sup>
Exp: Luong and Touati (1983)	0.17	0.54	0.94	2.69	13.6	17.1
Exp: Seif El Dine et al. (2010)	0.21	0.54	0.94	2.65	13.4	16.9
NE34 FS: Ciantia et al. (2018)	0.21	0.51	0.9	2.65	13.7	17.2

633 Note:  $D_{50}$ , mean grain size;  $e_{min}$ , minimum void ratio;  $e_{max}$ , maximum void ratio;  $\rho_s$ , specific gravity;  $\rho_{d,min}$ ,  
634 minimum dry density;  $\rho_{d,max}$ , maximum dry density

635

636 Table 2 DEM contact model parameters

Material	$G$ : GPa	$\mu$	$\nu$
F-Sand	9	0.28	0.2
Rod	77	0.3	0.52

637

638

639 Table 3 Geometrical characteristics of the virtual calibration chamber

Variable (unit)	Symbol	DEM
Chamber diameter (mm)	$D_c$	760
Rod outside diameter (mm)	$d_c$	50.8
Chamber height (mm)	$H$	500
Scaling factor	-	79
mean element size (mm)	$D_{50}$	16.6
Chamber/rod diameter ratio	$D_c / d_c = R_d$	15
Rod/particle ratio	$d_c / D_{50} = n_p$	3.06

640

641

642 Table 4 Some characteristics of previous calibration chamber studies of SPT

Researchers	Range of $D_r$ /%	Range of $P_0$ / kPa	Range of $N$	Container size	Radial BC	$D_{50}$ / mm	Proposed equation
Gibbs and Holtz /, Meyerhof (1957)	15-105	0-276	2-73	$D_c=90$ cm $H=120$ cm	Steel wall	1.58	$N = 1.7 \times \left(\frac{D_r}{100}\right)^2 (0.145P_0 + 10)$
Marcuson and Bieganousky (1977)	35-75	69-552	6-26	$D_c = 122$ cm $H=183$ cm	Steel/rubber wall	0.23	$N = -5.5 + 0.2(0.145P_0) + 0.0046(D_r)^2$
Yamada et al. (1992)	24-89	49-294	10-37	$D_c = 50$ cm $H=70$ cm	Triaxial cell	0.2	$N = 3.0 \times \exp(0.023D_r) \times \left(\frac{P_0}{98.1}\right)^{(1-0.0035D_r)}$
Ishikawa et al. (2013)	68-96	150-600	10-21	$D_c = 58.4$ cm $H=70$ cm	Steel wall	0.54	$N = \exp(2.21 \ln D_r + 0.646 \ln P_0 - 10.437)$

643

644

645

646

647

648

Table 5 Parameters describing the simulated driving system

$\rho_r$ (kg/m <sup>3</sup> )	$E$ (GPa)	$c$ (m/s)	$m_h$ (kg)	$h$ (m)	$g$ (m/s <sup>2</sup> )	$a$ (m <sup>2</sup> )	$A_h$ (m <sup>2</sup> )	$r$ (-)	$L$ (m)	$l$ (m)	$t_{\max}$ (ms)	$F_{\max}$ (kN)
8,050	200	4,984	63.5	0.76	9.8	0.002	0.008	0.25	0.97	10	4	251

649

650

651

Table 6 Basic programme of DEM-based dynamic probing tests

Test ID	$D_r$ : %	$P_0$ : kPa	N. of particles
Very Dense_100	82.6	100	69,166
Very Dense_200	83.0	200	69,166
Very Dense_400	83.7	400	69,166
Dense_100	74.0	100	66,059
Dense_200	74.7	200	66,059
Dense_400	75.7	400	66,059
Medium_100	62.1	100	60,031
Medium_200	62.9	200	60,031
Medium_400	63.9	400	60,031
Loose_100	40.7	100	50,335
Loose_200	41.7	200	50,335
Loose_400	43.2	400	50,335

652

653

Table 7 Results of DEM-based dynamic probing tests

Test ID	$v_{\text{peak}}$ : m/s	$q_d$ : MPa	$\Delta\rho$ : cm	$N$	$E_{\text{blow}}$ : J	$ER$ : %	$N_{60}$	$N/D_r^2$	$N_{60}/D_r^2$
Very Dense_100	1.37	9.45	0.67	44	196	41.5	31	66	45
Very Dense_200	1.26	15.76	0.36	83	199	42.1	58	123	84
Very Dense_400	1.31	21.64	0.24	123	200	43.0	87	184	124
Dense_100	1.42	5.39	1.45	21	203	42.9	15	36	24
Dense_200	1.35	10.19	0.7	42	197	41.7	30	82	53
Dense_400	1.30	14.62	0.31	97	179	38.1	61	186	107
Medium_100	1.42	4.56	2.27	13	213	45.1	10	36	25
Medium_200	1.35	9.71	1.01	30	190	40.4	20	82	50
Medium_400	1.38	10.33	0.5	60	189	40.0	40	166	98
Loose_100	1.47	1.56	5.63	5	270	57.1	5	35	30
Loose_200	1.40	3.09	2.54	12	221	46.7	9	77	53
Loose_400	1.35	7.72	0.93	32	196	41.5	22	212	119

654

655

656

657

658

659

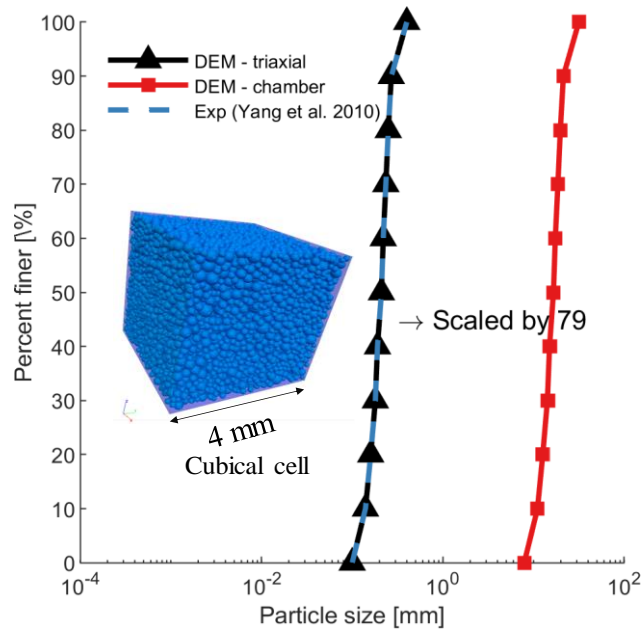
Table 8 Results from tests performed in similar conditions at different input energy

Test ID	$\eta_d$	$F_{max}$ : kN	$t_{max}$ : ms	$\Delta\rho$ : cm	$N$	$E_{blow}$ : J	$ER$ : %	$N_{60}$	$ER*N$
Dense_100_0.7	0.7	175.7	4	0.66	45	105	22.0	17	9.9
Dense_100_0.9	0.9	225.9	4	1.14	26	163	34.5	15	9.1
Dense_100	1.0	251	4	1.45	21	203	42.9	15	9.03
Dense_100_1.2	1.2	301.2	4	2.05	15	292	61.9	15	9.3

660

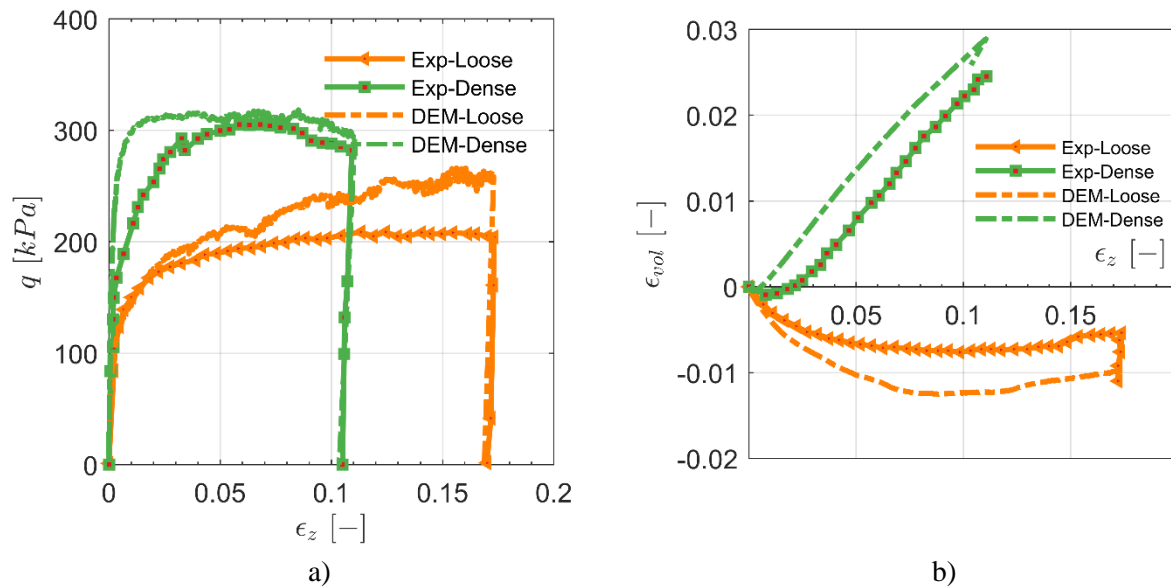
661

662 **9. Figures**



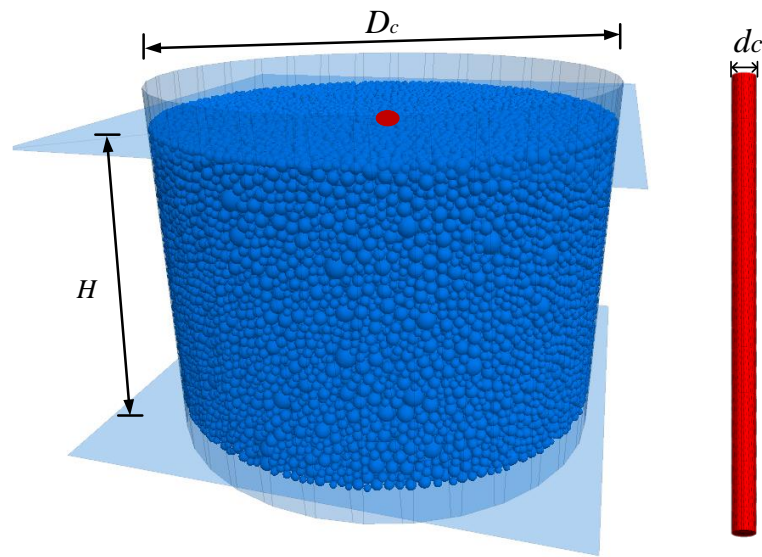
663  
664  
665

Figure 1 Particle size distribution of Fontainebleau sand and DEM models



666 Figure 2 Contact model calibration ( $G$ ,  $\mu$ ,  $\nu$ ) with triaxial tests on Fontainebleau sand from Seif El Dine et  
667 al. (2010): a)  $q$  vs  $\epsilon_z$ , b)  $\epsilon_{vol}$  vs  $\epsilon_z$ . Loose means at 30% relative density; dense at 70%

668

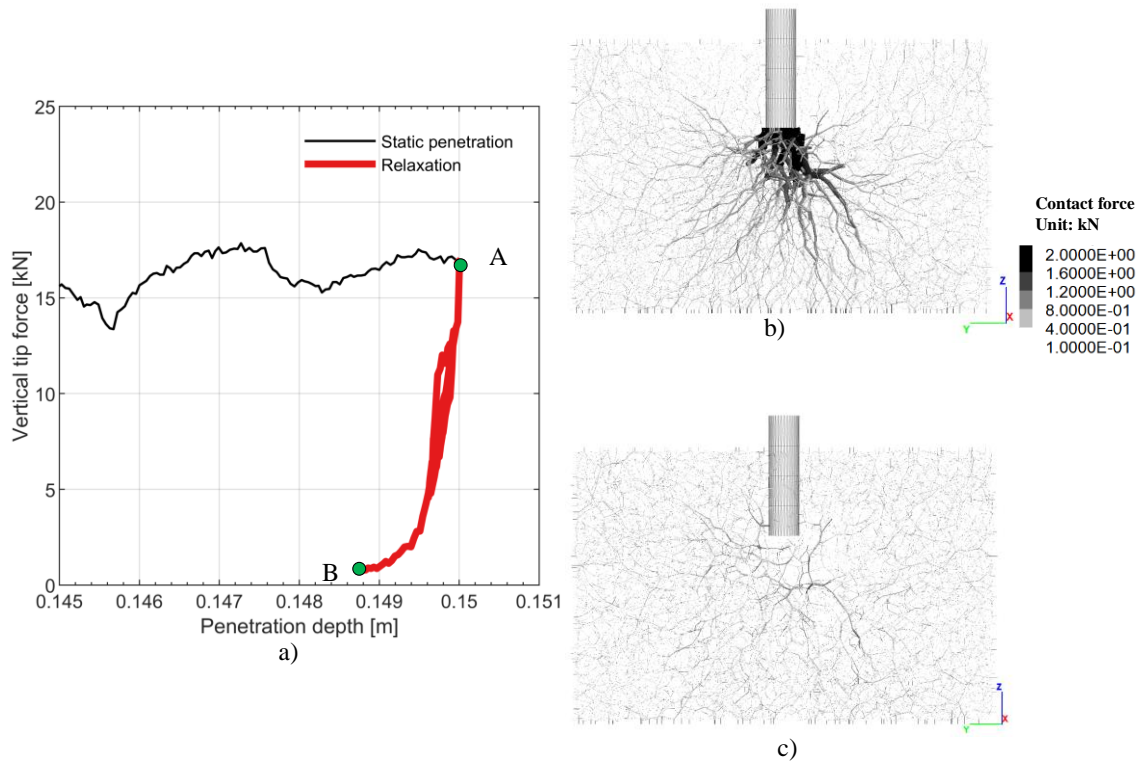


669

670

671

Figure 3 View of DEM model of calibration chamber and rod (flat-ended rod)



672

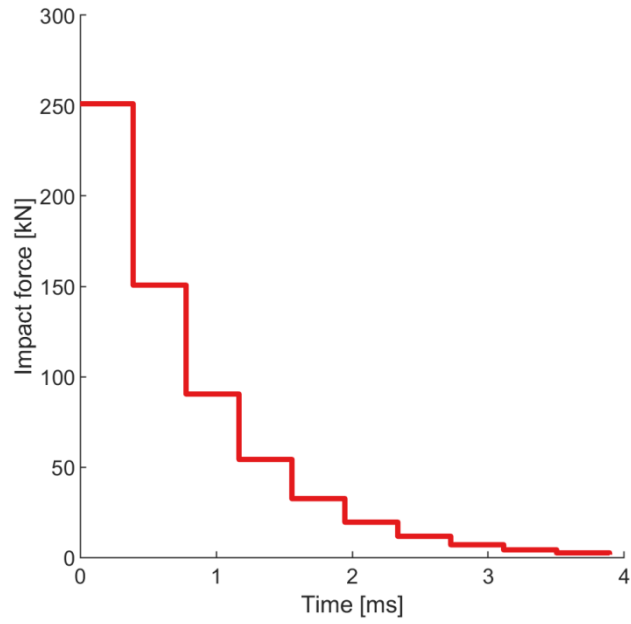
673

674

675

Figure 4. Residual force relaxation procedure (example: Loose\_400): a) reduction of rod-particle contact force; b) contact force network at point A; c) contact force network at point B

676

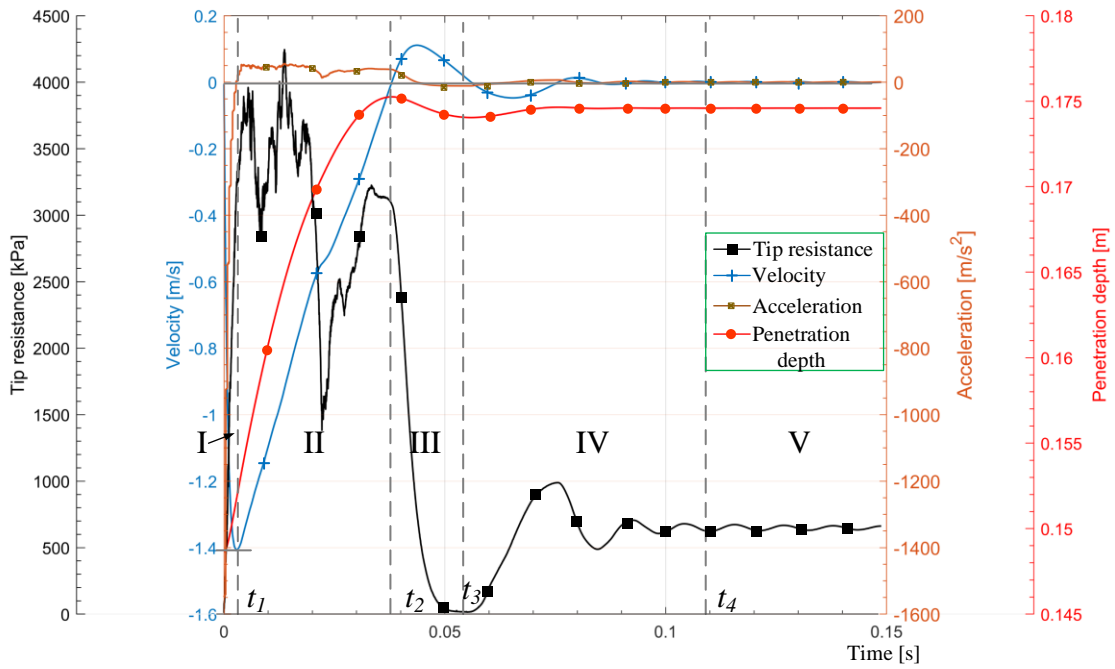


677

678

679

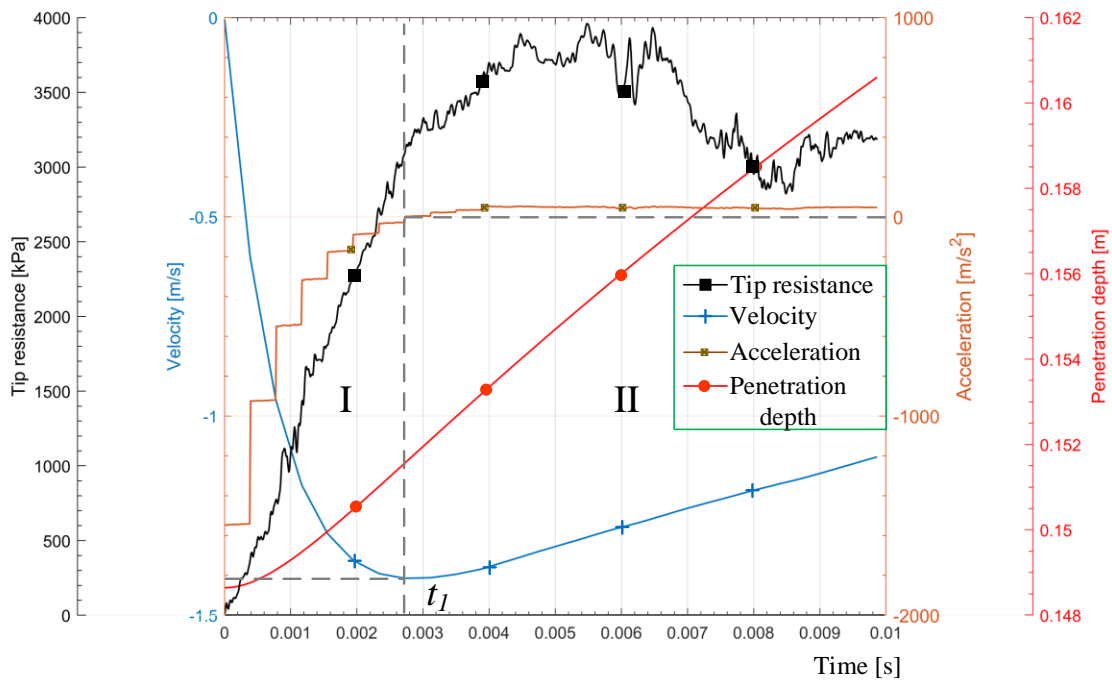
Figure 5 Base case for input driving force  $F_{drv}$



680

681

(a)



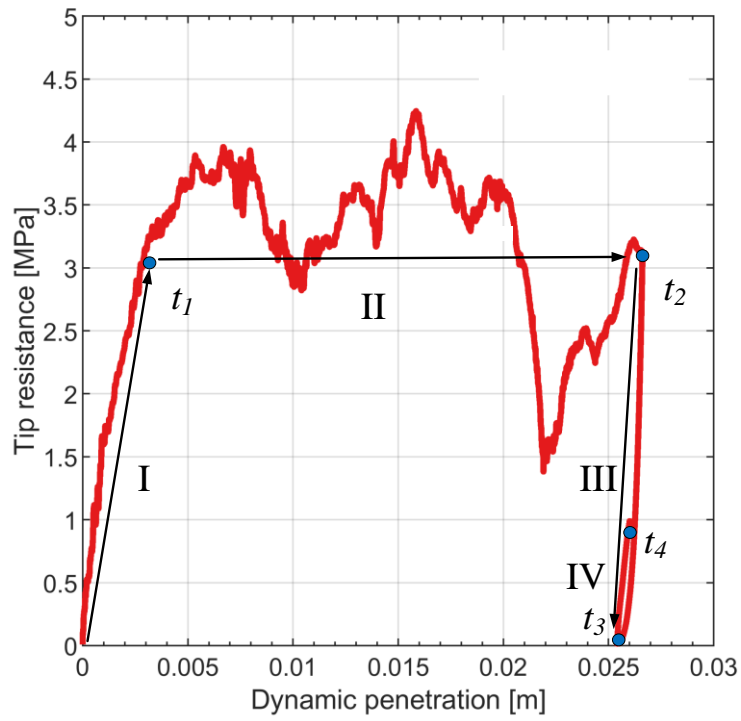
682

683

684

685

Figure 6 Evolution of tip resistance, rod velocity, rod acceleration and penetration depth during one impact with time in Test Loose\_200: (a) full analysis; (b) zoom-in view till 0.01s

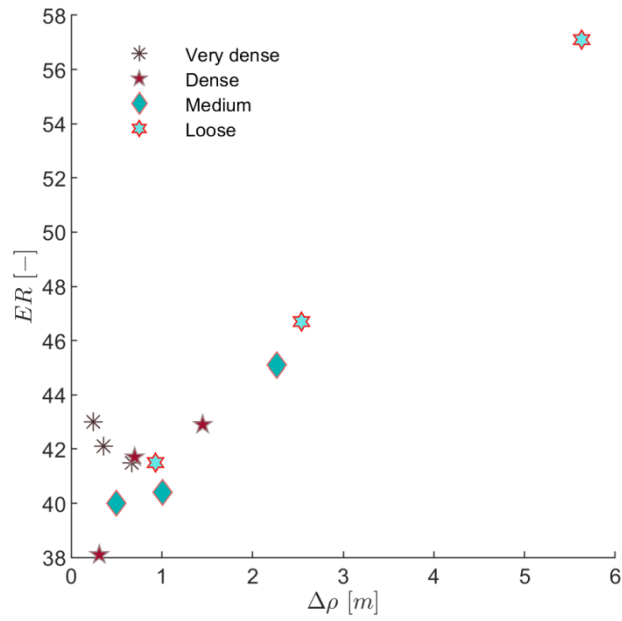


686

687

688

Figure 7 Example penetration curve during a blow (Loose\_200, Table 6)

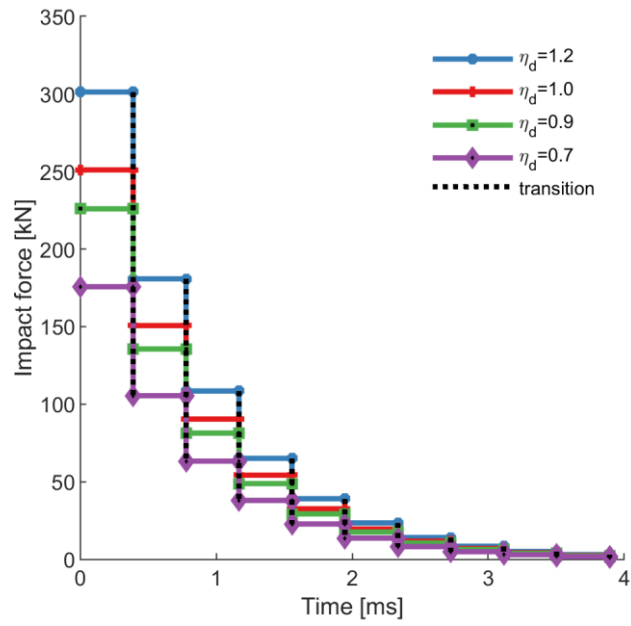


689

690

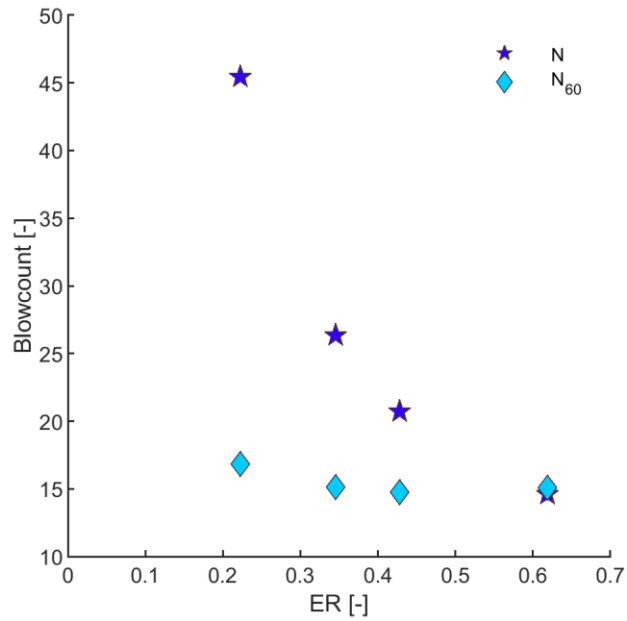
691

Figure 8 Energy input variations with blow depth



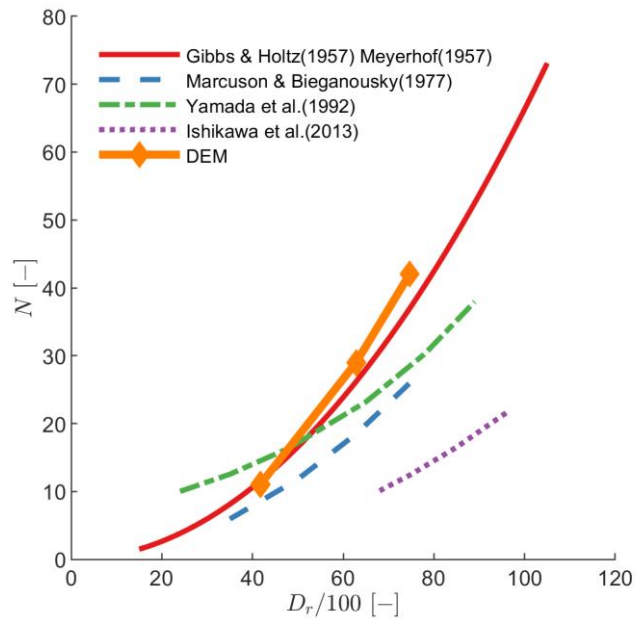
692  
693  
694

Figure 9 Various force-time input configurations



695  
696

Figure 10 Raw and normalized blow counts versus energy ratio observed in one single blow



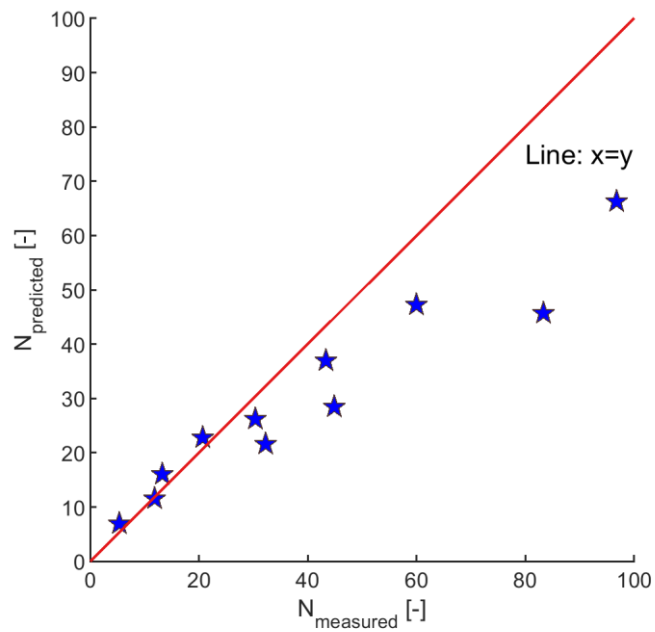
697

698

699

700

Figure 11 Relationship between  $D_r$  and penetration resistance at  $P_0= 200$  kPa

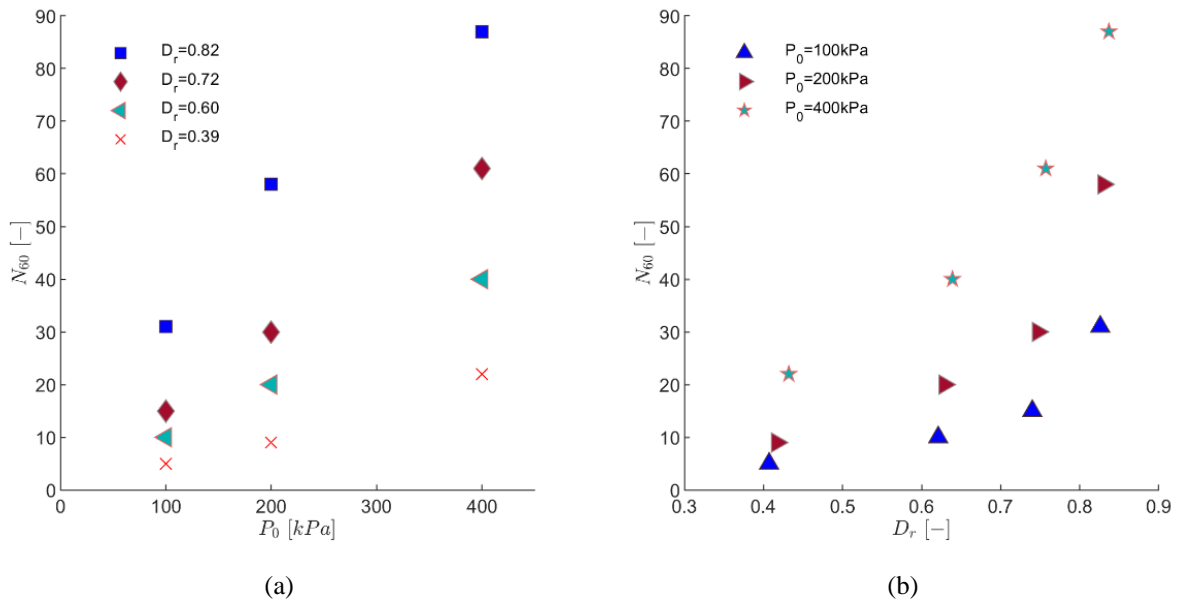


701

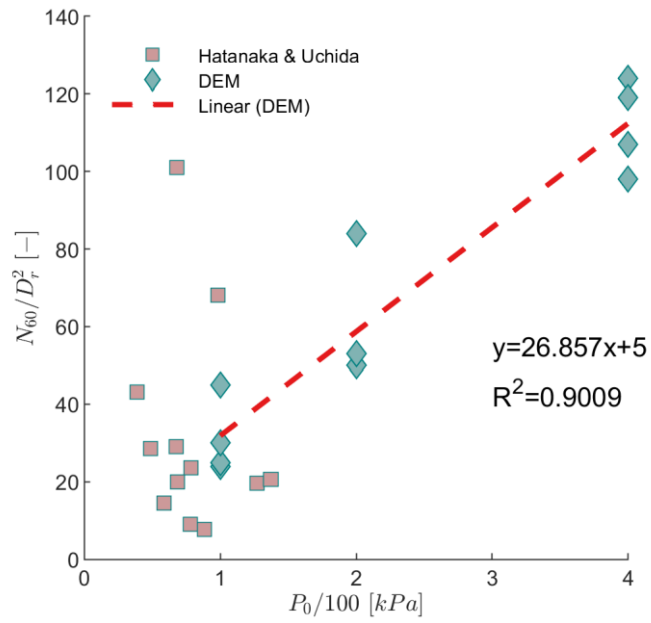
702

703

Figure 12 Measured blow numbers in SPT DEM simulation compared with those predicted by the Meyerhof expression (1957)

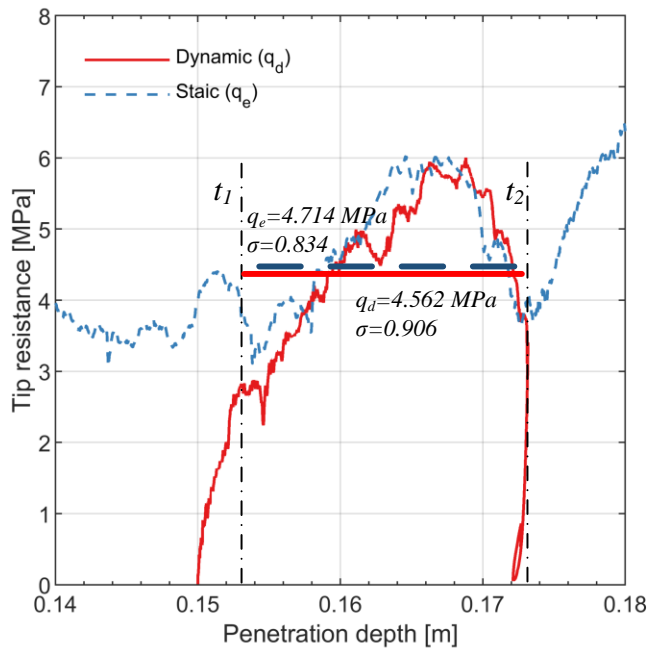


704 Figure 13 Influence of (a) overburden (b) relative density on the normalized blowcount estimated from the  
 705 simulations  
 706



707  
 708  
 709

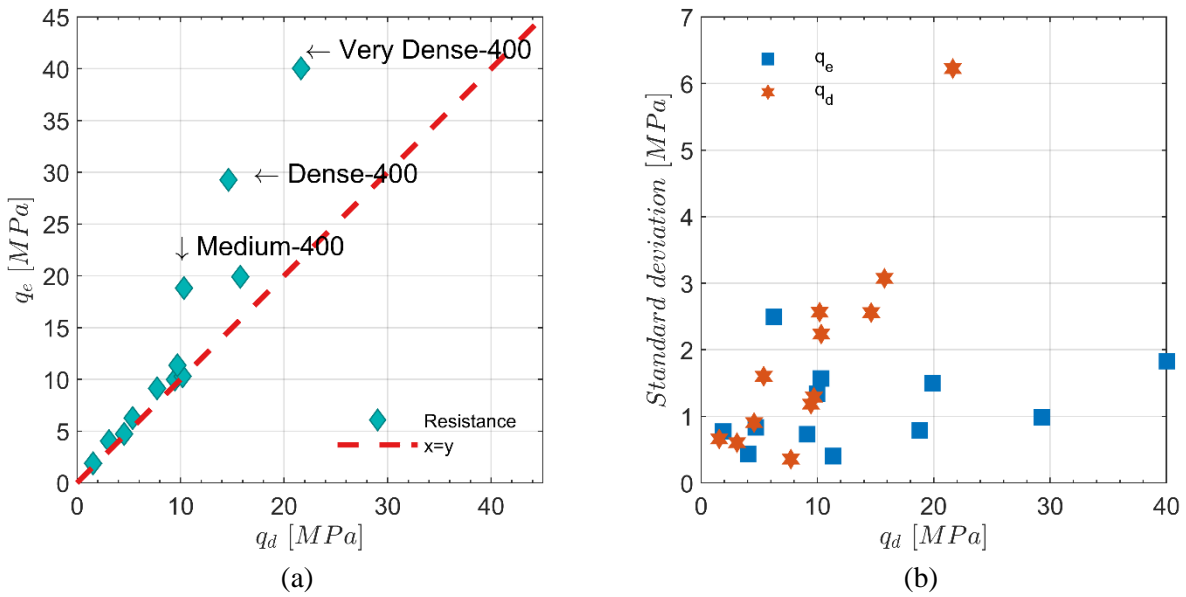
Figure 14 Comparison between normalized DEM results and test on frozen samples



710

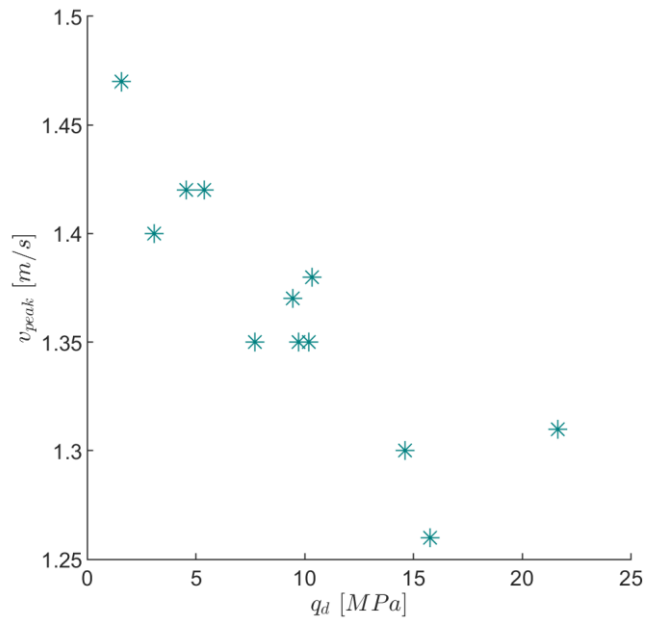
711

Figure 15 Example comparison of static and dynamic penetration (Medium\_100)



712

Figure 16  $q_e$  vs  $q_d$  and standard deviation of each case

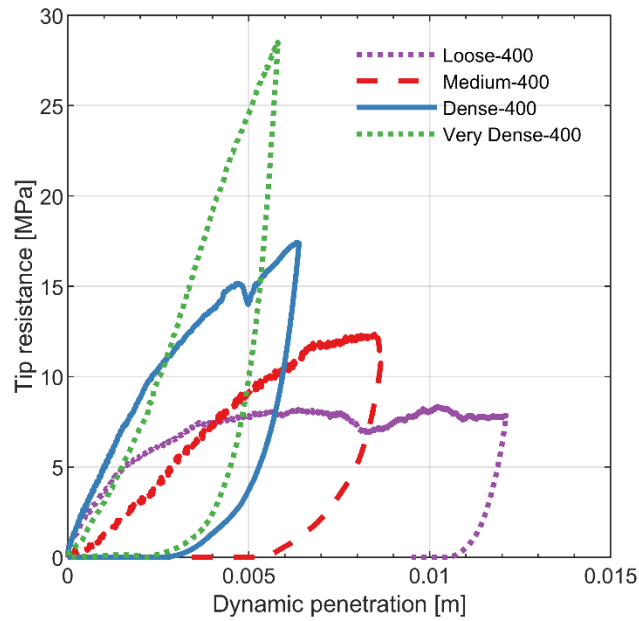


713

714

715

Figure 17 Peak velocity during dynamic probing vs average dynamic tip resistance



716

717

718

Figure 18 Influence of initial density on dynamic penetration curves for the series at  $P_0 = 400$  kPa